Heliyon 7 (2021) e08541

Contents lists available at ScienceDirect

Heliyon

journal homepage: www.cell.com/heliyon

Research article

Synthesis of hierarchical structured Gd doped α-Sb_2O_4 as an advanced nanomaterial for high performance energy storage devices

Vinayak Adimule [a,*], Basappa C. Yallur [b], Malathi Challa [b], Rajeev S. Joshi [c]

[a] Angadi Institute of Technology and Management (AITM), Savagaon Road, Belagavi 591108, Karnataka, India
[b] Department of Chemistry, M S Ramaiah Institute of Technology, Bangalore 560054, Karnataka, India
[c] School of Physical Sciences, Central University of Karnataka, Aland Road, Kadaganchi, Gulbarga, Karnataka 585311

GRAPHICAL ABSTRACT

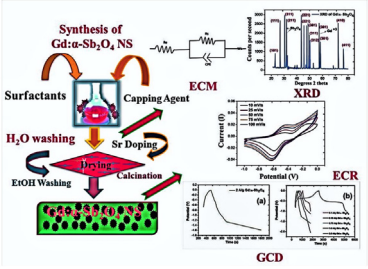

ARTICLE INFO

Keywords:
Nanostructures
Gd: α-Sb_2O_4
Super capacitor
Co precipitation
Energy storage devices

ABSTRACT

Bimetallic oxide nanostructures (NS) of Gd_x: α-Sb_2O_4 (x = 5, 8, 10 wt.%) emerged as novel electrode material for batteries as they exhibit large specific capacity and cyclic stability. Crystal structure of Gd: α-Sb_2O_4 NS investigated by X-ray diffraction (XRD) patterns and identified as mixed orthorhombic phase. Surface chemical composition, binding energies of the metal oxides and incorporation of Gd into α-Sb_2O_4 NS analysed by XPS (X-ray photoelectron spectral) studies. Microstructure analysis reveals that distinctive flower/flake like arrays with agglomeration. Morphology, structure and physical/chemical properties of the resulting nanostructure were analysed by SEM (scanning electron microscopy), SEM-EDX (scanning electron microscopy-energy dispersive X-ray), BET (Brunauer-Emmett-Teller), XPS, UV-Visible and XRD studies. Electrochemical performances of Gd_x: α-Sb_2O_4 (x = 10 wt.%) in 6 M KOH aqueous solution dipped in three electrode system evaluated by CV (cyclic voltammetry), GCD (galvanostatic charge-discharge) and EIS (electrochemical impedance spectroscopy) measurements. The as-synthesized NS exhibited higher specific capacitance of 958 mAh/g at a current density of 0.15 A/g and excellent cyclic stability with 86.5% capacitive retention after 1000 cycles. Distinctive flower/flake like structure, large surface area, and abundant active sites of Gd_x: α-Sb_2O_4 NS could be the reason for significant increase in charge transfer and storage. In brief this work offers facile method to synthesize Gd_x: α-Sb_2O_4 NS are promising electrode materials for potential applications in high performance super capacitor.

* Corresponding author.
E-mail address: adimulevinayak@yahoo.in (V. Adimule).

https://doi.org/10.1016/j.heliyon.2021.e08541
Received 19 May 2021; Received in revised form 8 August 2021; Accepted 30 November 2021

1. Introduction

Global energy demand leads to the development of batteries, fuel cells, super capacitors, solar cells for extensive range of applications. Super capacitors drawn much interest due to their high power output, extensive reversibility and exceptional cyclic stability [1, 2]. Super capacitor bridges the gap between conventional capacitor and batteries due to their high power density and specific capacitance. Many nanomaterials reported in literature for super capacitor properties and exploring the hybrid nanomaterials for high performance energy storage devices is a key interest in the present scenario [3, 4]. In electrochemical processes the term "pseudo capacitance" [5] is used to describe the behaviour of the electrode materials that has signature of capacitance electrode (such in case of carbon electrodes). Two extreme types of behaviours were observed for the electrochemical energy storage devices when charged/discharged under constant current. In case of hybrid devices the charge/discharge curve looks capacitive since, it is a combination of capacitive (triangular shape) and Faradaic (plateau shape) electrodes. Thus "hybrid" energy storage devices with different energy storage behaviour act as capacitive and Faradaic. The resulting electrode system is in between super capacitor and a battery. Zheng and Conway [6, 7] reported a maximum energy density in Sb composites with large surface area, flexibility, electrical conductivity which demonstrated 50 Wh/kg for activated carbon/Ni $(OH)_2$ in 6.25 M KOH solution [8, 9]. Theoretical capacity of the post transition metal oxides are usually high (>600 mAh/g) [10], such as α-Sb_2O_4 [11], Sb_2O_3 [12], Sb_6O_{13} [13]. Theoretical capacity of the Sb_2O_4 is much higher (1227 mAh/g) as compared with other analogues of antimony [14]. According to recent investigations Sb_2O_4 accommodates Na ions and forms alloy mixtures during electrochemical reactions. Sun *et al* [15] reported high capacitance of 1120 mAh/g for anode material of Sb_2O_4/Na NS [16]. It is extremely important to overcome the shortcomings of α-Sb_2O_4 anode material, among many other forms Sb_2O_4 exists in orthorhombic phase (α-Sb_2O_4) and monoclinic structure (β-Sb_2O_4) [17]. Alpha form of Sb_2O_4 can be easily converted from Sb_2O_3 [18, 19] and can be used in oxidation of methane gas and sodium ion batteries [20]. Fu *et al* [20] studied thin film of Sb_2O_4 and determined reversible specific capacitance electrochemically (899 mAh/g). Alpha Sb_2O_4 synthesized effectively by hydrothermal method using urea and $SbCl_3$ as starting material. The material possesses band gap of 3.2 eV and studied for their photo catalytic activities and chemical sensing mechanism [21]. One dimensional Sb_2O_4 NS synthesized from bulk Sb and reported as advanced anode material for lithium ion batteries (LIBs) and sodium ion batteries (SIBs). One dimensional Sb_2O_4 NS even at high current density of 1000 mA/g, showed excellent cyclic stability and rate capability [22]. Electrochemical behaviour of α-Sb_2O_4 thin films deposited by magnetron spluttering displayed large reversible capacity of 896 mAh/g and material can be used as high energy storage device applications especially in sodium ion batteries [23]. Sb_2O_4: rGO [24] synthesized by solvothermal approach with specific capacity of 1170 mAh/g at 100 mA/g and studied widely as anode material in lithium ion batteries. Recently Cd doped Sb_2O_4 NS synthesized by wet chemical process and studied for the detection of melanin from aqueous solution electrochemically [25]. Generally bimetallic oxides exhibit promising results when incorporated in electrochemical studies. Gd_2O_3/Gd^{+3} when doped with different NS behave as conducting material in nature due to non-stoichiometric distribution of oxygen vacancies [26, 27]. The conducting nature of bimetallic oxides are due to the formation of metal intestinal structure, defects and formation of oxygen vacancies in the doped NS as compared with undoped NS. Two dimensional hexagonal $CoMoO_4$ nano sheets grown on a conductive carbon fabric cloth behave as pseudo capacitor which exhibited maximum specific capacitance of 1210 F/g at 2.5 A/g with cyclic stability of 91% after 10000 cycles [28]. Super capacitor performance of flower shaped $CoNi_2S_4$ synthesized on Ni-foam exhibited specific capacitance of 2300 F/g at 1 mA/g with excellent cyclic stability of 93.8% after 5000 charge-discharge cycles [29]. Novel gravel shaped $NiMoO_4$ NPs dispersed over carbon cloth binder free material for super capacitor applications unveils specific capacitance of 970 F/g at current density of 2.5 A/g with exceptional cyclic stability and retention of 91.34% after 5000 cycles [30].

Here in we report the co precipitation method of synthesis of Gd_x (x = 5, 8 and 10 wt.%): α-Sb_2O_4 NS with superior electrochemical properties. Gd: α-Sb_2O_4 NS synthesized by co precipitation method and characterized by XRD, SEM, UV-Visible, BET, EDS (energy dispersive spectroscopy) and XPS spectroscopic investigations. Notably, Gd: α-Sb_2O_4 NS (10 wt.%) in 6 M KOH aqueous solution demonstrated specific capacitance of 958 mAh/g at a current density of 0.15 A/g with capacitance retention rate of 86.5% after 1000 cycles.

1.1. Materials and methods

All the required chemicals and reagents were commercially available and procured from Sigma Aldrich, Alfa Assar, S-d fine Ltd. and used without further purification. $SbCl_3$ (>98.5% purity, Spectro chem Ltd., India), urea (>99% purity, S-d fine chemicals Ltd., India), NH_4OH (38% aqueous solution, S-d fine chemicals Ltd.), Gd_2Cl_3 (>98.5% purity, Sigma–Aldrich, India). Deionized water was used throughout the experiments to avoid contamination. Advanced powdered X-ray diffractometer (XRD) rigaku miniflex bench top instrument operated at 600 W power fitted with X-ray tube functioning at 50 Hz/60 Hz frequency (CuKα radiation. λ = 0.15406 nm) and scanning angle of 20–80° (2θ) and XPS PHI Versa Probe (III) instrument having Ar ion as well as C 60 sputter guns were used for the analysis of crystal structure, phase purity and surface chemical oxidation states. Specord 250 plus instrument and with coolant built in the instrument and Nova Nano-SEM 450 equipped with 5 X to 1,000,000 X HR/UHR modes, high sensitivity, low kV directional backscattered detector (DBS), scanning electron microscope (SEM) were applied to analyze the optical absorptivity, structural morphologies and particle size respectively. IXRF system with model 550i pulse detector consisting of ultrafast X-ray processing unit and NOVA 1200 e instrument having samples degreased at 200 °C before N_2 adsorption were applied to investigate quantitative chemical composition, pore size, pore diameter, surface area of the as-synthesized nanostructures. Electro analysis was carried out using Sinsil International 1200 C instrument and studied galvanostatic charge and discharge cycles (GCD), cyclic stability, energy storage properties of Gd: α-Sb_2O_4 NS.

2. Experimental

2.1. Synthesis of α-Sb_2O_4 nanostructures (NS) (step 1)

Distinctive flower/flake like NS of Gd: α-Sb_2O_4 synthesized by facile co precipitation method. In a typical process, 0.1 M $SbCl_3$ (0.1 M, 50 mL), 0.1 M urea (0.1 M, 50 mL) were dissolved in 20 ml of deionised water kept under continuous stirring for 1–2 h. Then NH_4OH solution was added drop wise at room temperature, followed by heating at 80 °C for 8 h. After cooling to normal temperature, off-white coloured precipitate (Eq. (1)) was taken out, washed with cold water (30 ml × 3 times), acetone (20 ml × 3 times) and dried at 100–200 °C, finally calcinated at 700–800 °C for 24 h [31].

Reactions

$$Sb_2Cl_3 + 4H_2O + H_2O \rightarrow Sb_2O_4 + 3H_2\,(g) + 3HCl\,(g) + OH^-\,(aq) \quad (1)$$

2.2. Gd doping to α-Sb_2O_4 nanostructures (step 2)

0.1 M Gd_2Cl_3 (2.68 g) (Gd_x where, x = 5, 8 and 10 wt.%) dissolved in 50 ml of 0.1 M aqueous urea solution, 2 ml of triethanol amine and heated at 80 °C for 4h. To the hot solution, α-Sb_2O_4 (step 1) was added and continued heating at 80 °C for 10 h. After cooling to normal temperature, aqueous NH_4OH was added drop wise under continuous

stirring. White coloured precipitate (Eq. (2)) was taken out washed with cold water (50 ml × 3 times), acetone (10 ml × 2 times) and ethanol (20 ml × 2 times) and dried at 100–200 °C, finally calcinated at 750–800 °C for 36 h. Schematic synthetic pathway presented in Figure 1.

Reactions

$$Gd_2O_3 + 2\,Sb_2O_4 + H_2O \rightarrow 2\,Gd:\ \alpha - Sb_2O_4 + 2\,O_2\,(g) + H_2\,(g) \quad (2)$$

2.3. Elemental compositional analysis of Gd: α-Sb_2O_4 NS

Purity and chemical composition of the NPs were investigated in order to understand distribution inside Gd: α-Sb_2O_4 NS. The elemental composition analysis aims to understand the chemical constituents of metal or non-metals and the experimental set up needed for their analysis. Gd: α-Sb_2O_4 NS formed via co precipitation method, during the formation solvent and metal ions in solution react with each other to form metal oxide semiconductor (MOS) NPs. Percentage composition of the Gd: α-Sb_2O_4 NS and their purity are summarized in Table 1.

3. Results and discussions

3.1. XRD studies

The crystalline nature of the electrode Gd_x: α-Sb_2O_4 examined by XRD (X-ray diffractometer) analysis and corresponding pattern is displayed in Figure 2. Crystal structure was determined using source of monochromatic CuKα radiation (λ = 0.15406 nm, 40 kV, 50 Hz), scanned in step of 0.03° with angular range of 20–80° (2θ). High purity and crystalline phase of orthorhombic Gd_x: α-Sb_2O_4 NS confirmed by sharp and intense diffraction pattern. The crystallographic structure and d-spacing (hkl) are compared with reported values of α-Sb_2O_4 and are in good agreement with each other [32, 33]. The diffraction peaks/planes of as-synthesized Gd_x: α-Sb_2O_4 NS (as shown in Figure 2(a) appear at 23.2° (101), 26.4° (111), 31.8° (311), 33.2° (211), 35.4° (201), 44.1° (221), 46.2° (221), 46.8° (301), 48.1° (311), 48.6° (311), 50.8° (312), 58.1° (301), 59.2° (301), 73.4° (410), 76.8° (411) and the diffraction peaks/-planes of pure α-Sb_2O_4 NS (as shown in Figure 2(b) appear at 23.2° (101), 26.4° (111), 31.8° (311), 33.2° (211), 35.4° (201) respectively). These peaks/planes of the as-synthesized Gd_x: α-Sb_2O_4 NS accurately matches with orthorhombic phase of Sb_2O_3 NS with standard JCPDS card # 71-0383. Sharp peaks and lack of impurity peaks were observed, suggesting high purity and crystallinity of the NS. For all the NS, lattice parameters are calculated using Debye-Scherrers formula [34]. As result of Gd^{+3} ions doped into α-Sb_2O_4 NS which apparently causes crystal lattice distortion and reduction in Gd^{+3} ion concentrations. The Gd^{+3} ionic radius (1.05 Å) is smaller than the Sb^{+2} atomic radius (1.67 Å) as a result of lanthanide contraction and cell volume decreases since, more Gd^{+3} ions getting replaced into α-Sb_2O_4 NS [35]. G. Vijayaprasath *et al* [36] studied sharp diffraction peaks/planes of Gd doped ZnO NS and found that increase in unit cell volume as a result of decrease in intensity of the reflection peaks and increase in FWHM (full width half maximum) value. More importantly low crystallinity in nano scale is common occurrence in co precipitation method [37]. The scan step is measured in 2θ (0.02) and scan speed is measured in seconds or degrees per minutes. The detector has 176 active channels with a step size of 0.02° and scan speed was adjusted to 0.1 s in the total swift of the angle between 20–80°. It would account for 4000 steps and require 17.6 × 4000 s. Table 2 presents d-spacing, 2θ, FWHM of the as synthesized Gd: α-Sb_2O_4NS. The crystallite size, texture coefficient, morphology index and relative percentage error were summarized in Table 3. Crystallographic size decreases as Gd concentration increases which reveals well dispersion of the Gd NPs [38]. The obtained XRD planes matches with the JCPDS file No 71-0383 and the reported literatures [39, 40]. The d-spacing of the respective peaks/planes, average particle size, and crystallinity are calculated using Debye-Scherrers formula (Eq. (3))

$$D = K\lambda/\beta\,Cos\,\theta \quad (3)$$

Table 1. Elemental compositional analysis of Gd_2O_3, α-Sb_2O_4 and Gd: α-Sb_2O_4 NS.

Nanostructures	Sb	Gd	Na	O	K	Purity
Gd_2O_3	0.05	95.8	1.02	1.90	0.27	99.04
α-Sb_2O_4	95.9	0.09	1.12	1.59	0.21	98.91
Gd: α-Sb_2O_4	85.94	11.22	0.47	1.64	0.21	99.48

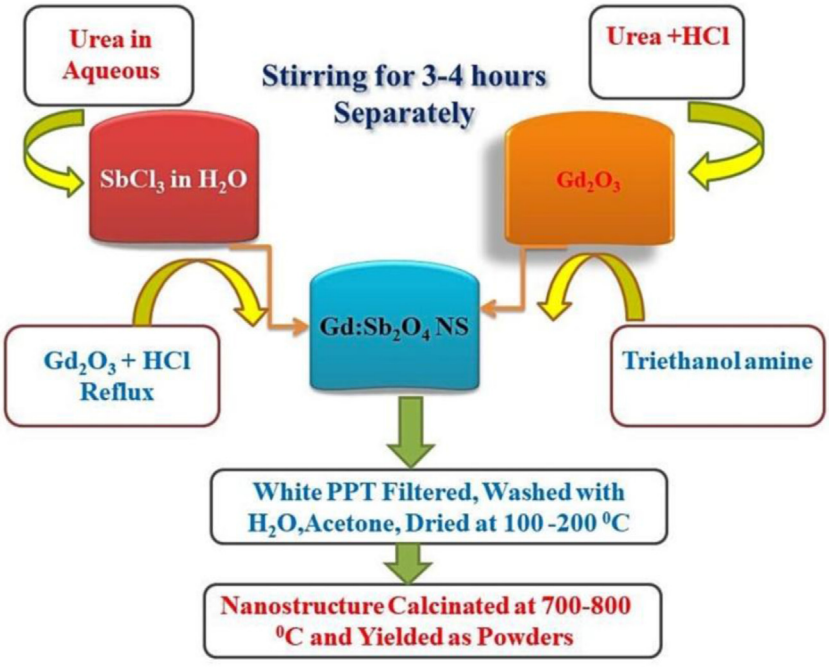

Figure 1. Schematic synthetic pathway of Gd_x: α-Sb_2O_4 NS.

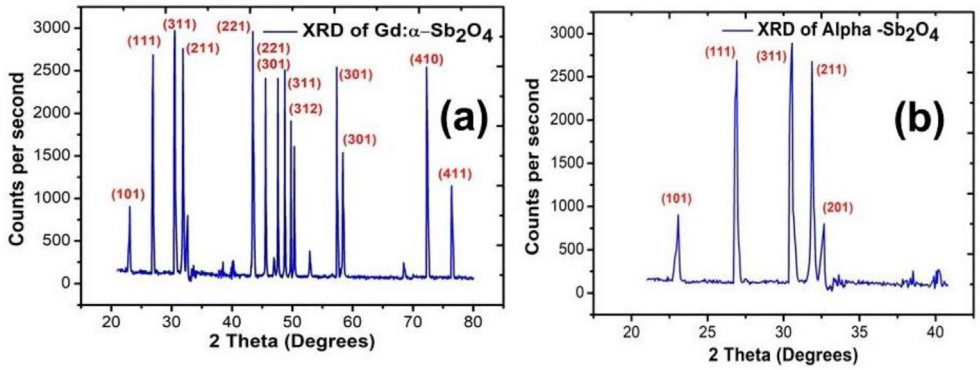

Figure 2. XRD diffraction patterns of (a) Gd: α-Sb_2O_4 (10 wt.%) NS and (b) pure α-Sb_2O_4 NS.

Table 2. Angle shift, d $_{(hkl)}$, lattice parameters, FWHM and crystallite size (D) obtained from XRD analysis of Gd: α-Sb_2O_4 (10 wt.%) NS.

Nanostructures	2θ	d $_{(hkl)}$ (Å)	FWHM (°)	Lattice parameters	Angle shift Δ 2θ (°)
Gd: α-Sb_2O_4 (5 wt.%)	35.45	2.835 (311)	0.2200	a = 0.2455 ± 0.11, b = 0.2389 ± 0.22, c = 0.2129 ± 0.52	0.21
Gd: α-Sb_2O_4 (8 wt.%)	35.41	2.836 (311)	0.2345	a = 0.2224 ± 0.47, b = 0.2029 ± 0.32, c = 0.211 ± 0.12	0.24
Gd: α-Sb_2O_4 (10 wt.%)	35.43	2.837 (311)	0.2161	a = 0.2784 ± 0.14, b = 0.2627 ± 0.87, c = 0.21489 ± 0.46	0.22

Where, D-average crystalline size, K-shape factor (0.89 for Cu-Kα radiation), λ -wavelength of X-ray, θ-full width of the diffraction angle (FWHM).

3.2. UV-visible spectral studies

Optical properties of Gd: α-Sb_2O_4 NS (5 wt.%, 8 wt.% and 10 wt.%) displayed in Figure 3. Optical properties related to the outermost electrons of an atom or molecule which absorb radiant energy of particular wavelength and undergo transition to higher energy level. In this process of excitation, energy gap of the material can be determined. Optical absorbance was carried out at ambient condition. Gd: α-Sb_2O_4NS (5 wt.%) as displayed in Figure 3(a) exhibit maximum absorbance (λ_{max}) of 335 nm, shoulder peak centred at 351 nm. Further, Gd: α-Sb_2O_4NS (8 wt.%) as displayed in Figure 3(b) revealed maximum absorbance (λ_{max}) appeared at 330.3 nm, shoulder peak formed at 348.5–364.3 nm. In addition, Gd: α-Sb_2O_4NS (10 wt.%) maximum absorbance spectrum (λ_{max}) centered at 328 nm and shoulder spectrum formed between 345 nm–356 nm. The entire spectrum doesn't show any peaks in between 400–600 nm Figure 3(c) shows overlay of optical absorbance spectrum and blue shift in the entire spectrum appeared in the wavelength range of 335 nm–328 nm (Figure 3(d)). The blue shift in UV-Visible spectrum of Gd_x: α-Sb_2O_4 NS is due to overloading of Gd^{+3} ions which intern creates lattice defects and facilitate easy transfer of oxygen ions and electrons to the surface of the nanomaterials [41, 42]. In order to calculate the optical band gap of the NS a plot of $(\alpha h\gamma)^2$ versus incident photon energy (hγ) has been drawn intercepting X-axis as shown in Figure 4. The optical band gap was calculated by extrapolation of the straight line drawn from the plot of $(\acute{\alpha}h\gamma)^2$ Vs (hγ) and extended it to the zero absorption coefficients. From the graph (Figure 4) optical band gap of Gd: α-Sb_2O_4 NS (10 wt.%) was found to be 3.16 eV [43]. The band gap of the samples recorded and calculated by Kubelka-Munk model and the allowed optical transference was calculated using the below formula (Eq. (4))

$$(\alpha h\gamma)^2 = C\,(h\gamma - Eg) \tag{4}$$

Where, C-absorption coefficient, hγ-photon energy and E_g-optical band gap, α-absorption coefficient. Optical absorption coefficient can also be calculated using the below formula (Eq. (5))

$$\alpha = \frac{1}{d\log\,(1|T)} \tag{5}$$

Where, α-absorption coefficient, d-thickness of the thin films and T-optical transmittance. Comparison of optical absorptivity data of Gd_2O_3, α-Sb_2O_4 and Gd: α-Sb_2O_4 NS (5, 8 and 10 wt.%) summarized in Table 4.

Table 3. Crystallite size, morphology index, relative percentage error (RPE) and texture coefficient (TC) values of Gd: α-Sb_2O_4 (10 wt.%) NS.

Nanostructures	Crystallite size (Å)	Morphology index t (D)	Relative percentage error (RPE)	Texture coefficient (TC)
Gd: α-Sb_2O_4 (5 wt.%)	38.312	1.240	0.01835	0.925
Gd: α-Sb_2O_4 (8 wt.%)	46.881	1.249	0.01848	0.921
Gd: α-Sb_2O_4 (10 wt.%)	49.477	1.220	0.01896	0.954

3.3. X-ray photoelectron spectroscopic studies (XPS)

Chemical constituents present in Gd: α-Sb_2O_4 electrode were investigated by X-ray photoelectron spectroscopy. The two distinct peaks for O1s as displayed in (Figure 5(a)) located at average binding energy of 529.6 eV assigned to the existence of O^{2-} [44, 45] and C1s core peak as displayed in (Figure 5(b)) located at average binding energy of 282.5 eV suggesting the presence of functional group related to oxygen in carbon ring skeleton. The distinct high resolution spectrum of Sb-3d exhibit two fittings (doublet separation of 11.1 eV) at 539.1 eV and 550.2 eV (Figure 5(c)) which are revealed to Sb $3d_{3/2}$ (Sb–O) and Sb $3d_{5/2}$ orbital respectively. Formation of Gd_2O_3 NS has been confirmed by high resolution two distinct spectrum of Gd-3d appeared at binding energies of 131.3 eV (strong peak) and 134.4 eV (weak peak) (Figure 5(d)) which are revealed to Gd $3d_{3/2}$ and Gd $3d_{5/2}$ and associated with Gd 3d orbital spin coupling (oxidation of Gd^{+3}) [46]. The full survey XPS spectrum (Figure 6(a)) displayed the presence of O. C, N, Gd, Sb peaks centred at

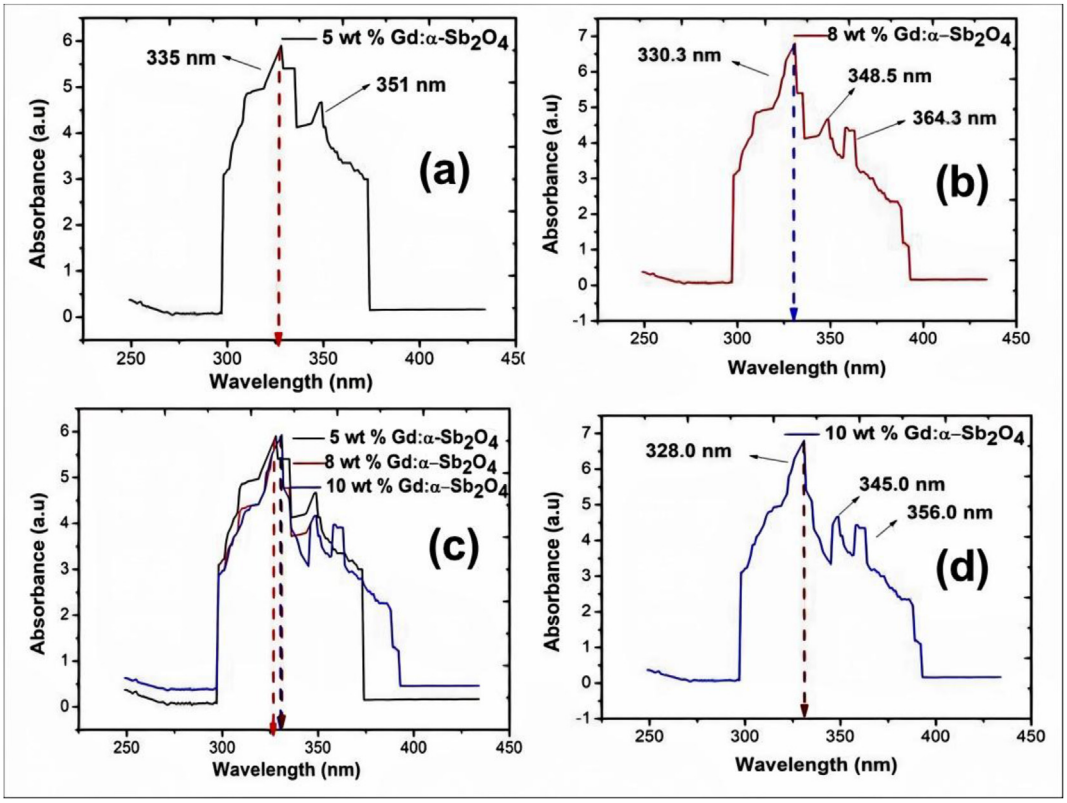

Figure 3. Optical absorbance of (a) Gd: α-Sb_2O_4 NS (5 wt.%) (b) Gd: α-Sb_2O_4 NS (8 wt.%) (c) Overlay spectrum and (d) Gd: α-Sb_2O_4 NS (10 wt.%).

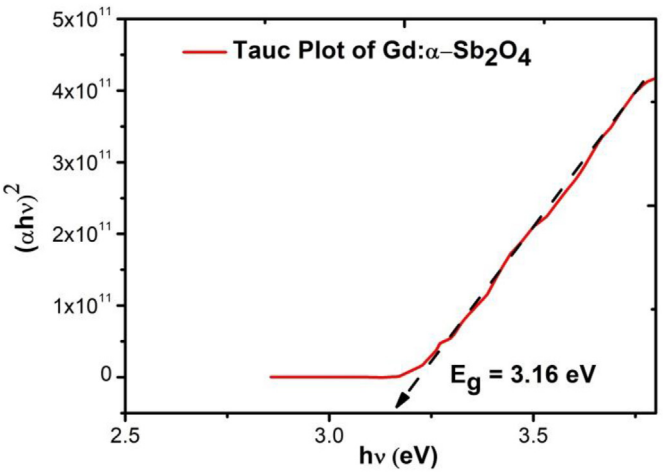

Figure 4. Optical energy band gap (Tauc's plot) of Gd: α-Sb_2O_4 NS (10 wt.%).

Table 4. Optical absorbance values of Gd_2O_3, α-Sb_2O_4 and Gd: α-Sb_2O_4 NS (5, 8 and 10 wt.%).

Nanostructures	λ maximum	λ shoulder 1	λ shoulder 2	Absorptivity Region
Gd_2O_3	340	–	–	Ultraviolet
α-Sb_2O_4	307	–	–	Ultraviolet
Gd: α-Sb_2O_4 (5wt.%)	335	351	–	Ultraviolet
Gd: α-Sb_2O_4 (8wt.%)	330.3	348.5	364.3	Ultraviolet
Gd: α-Sb_2O_4 (10 wt.%)	328	345	356	Ultraviolet

different binding energies. Interestingly high co-existence of O1s (Figure 6(b)) with Gd 3d oxidation states (broader satellite peaks) (Figure 6(c)) can generate more active sites for electrochemical reactions. Further, similar high co-existence can be found with C1s (Figure 6(d)) and Gd $3d_{3/2}$ and Gd $3d_{5/2}$ (Figure 6(e)) peaks. Moreover, co-existence of O1s (Figure 6(f)) with Sb 3d (Sb $3d_{3/2}$) (Figure 6(g)) oxidation states exhibit the formation of Sb–O–Sb bond well dispersed inside Gd: α-Sb_2O_4 NS which results to enhance energy storage and achieve high specific capacitance of Gd: α-Sb_2O_4 electrode. Separation of doublet and their binding energies of various elements are summarized in Table 5.

3.4. Energy dispersive X-ray spectroscopy (EDS) characterization

Energy-dispersive X-ray spectroscopy (EDS) was used to characterize the elemental composition of the synthesised Gd: α-Sb_2O_4 NS. EDS spectrum of pure α-Sb_2O_4 NS and Gd: α-Sb_2O_4 NS (10 wt.%) presented in Figure 7(a) and (b) respectively with inset table containing composition of elements. presence of Sb and Gd, thus confirming the bimetallic-nature of the material. The presence of Na, K, Cl, O and other trace elements in the material are impurities that resulted from the precipitation during the NS synthesis [47]. The Figure 7(a) results from the Sb wt.% were 72.16% and the O wt.% of 21.4% and Figure 7(b) Sb wt.% of 70.16%, Gd wt.% of 12.28%. Overall, the composition of Sb, Gd and O was observed to be preserved during experimentation, therefore demonstrating the chemically stability of the material.

3.5. BET studies

Brunauer-Emmett-Teller was used to analyse the surface area and porosity properties of the pure α-Sb_2O_4 and Gd: α-Sb_2O_4 (10 wt.%) NS as illustrated in Figure 8 and data summarized in Table 4. As illustrated in Table 4, BET analysis was used to characterise surface area and porosity properties of Gd: α-Sb_2O_4 NS. It was observed that the Gd: α-Sb_2O_4 (10 wt.%) NS showed a massive increase in the surface area of approximately 50 m^2/g to 151 m^2/g (increases upon doping) as compared with pure α-Sb_2O_4 NS in which surface area observed from 10 m^2/g to 60 m^2/g. Presence of C, H, O, Na, Gd and Sb are atoms which can play a significant

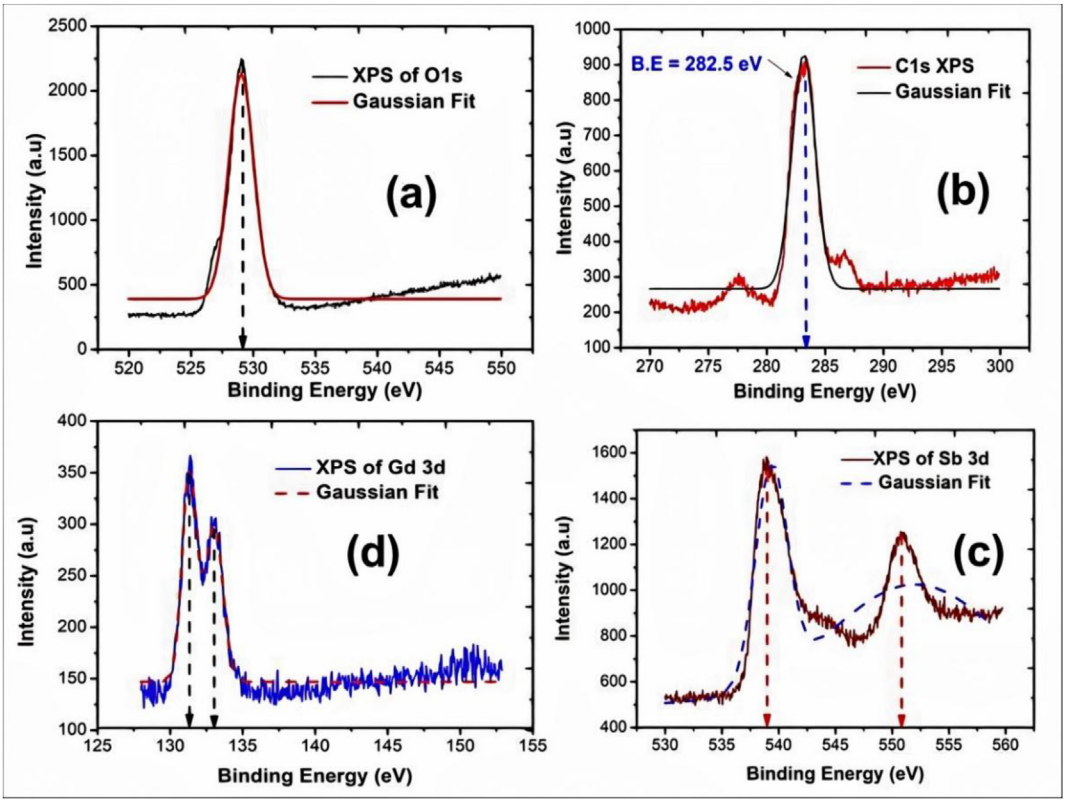

Figure 5. Binding energies and Gaussian fit graphs of (a) O1s (b) C1s (c) Sb $3d_{3/2}$ and Sb $3d_{5/2}$ (d) Gd $3d_{3/2}$, Gd $3d_{5/2}$.

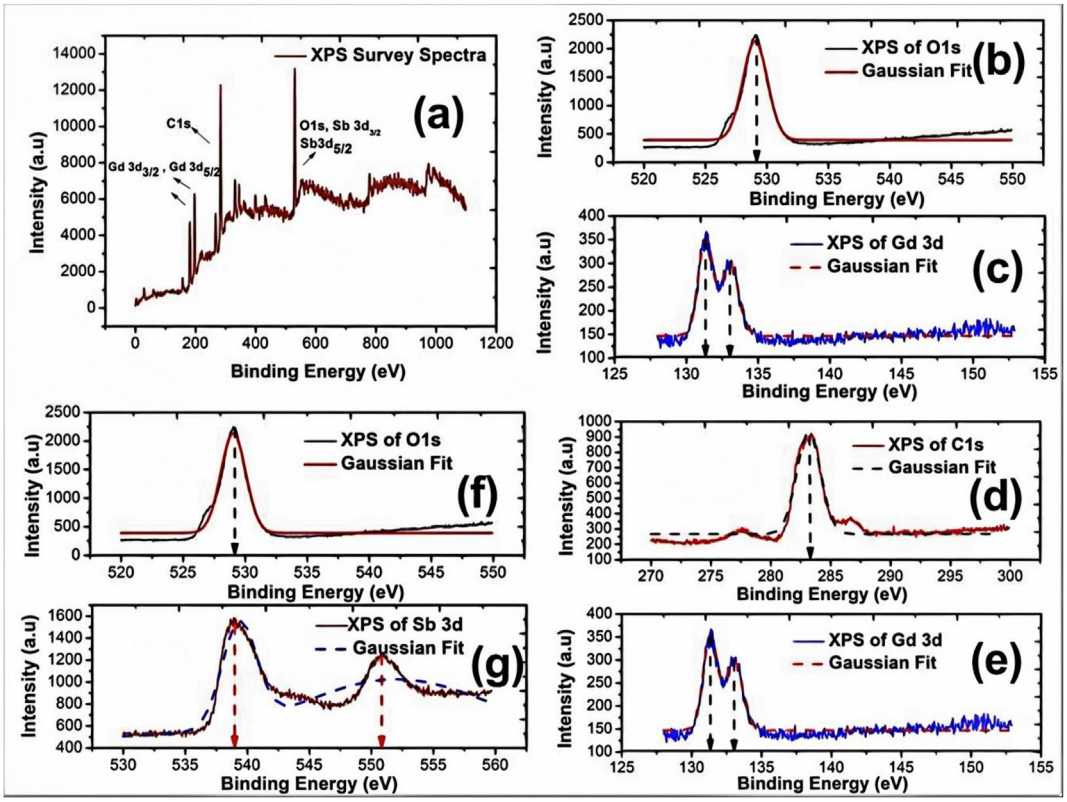

Figure 6. XPS of (a) Survey spectrum (b) and (c) Overlay of O1s with Gd $3d_{3/2}$, Gd $3d_{5/2}$ (d) and (e) Overlay of C1s with Gd $3d_{3/2}$, Gd $3d_{5/2}$ (f) and (g) O1s Overlay with Sb $3d_{3/2}$ and Sb $3d_{5/2}$ respectively.

Table 5. Binding energies of O1s, C1s, Sb $3d_{3/2}$, Sb $3d_{5/2}$, Gd $3d_{3/2}$, Gd $3d_{5/2}$ together with doublet separation.

Peak Assignment	Binding Energy (eV)	Separation of doublet (eV)
C1s	282.5	–
Gd $3d_{3/2}$	131.3	–
Gd $3d_{5/2}$	134.4	3.1
Sb $3d_{3/2}$	539.1	–
Sb $3d_{5/2}$	550.2	11.1
O1s	529.6	–

role in strengthening the Van der Waals forces of the material. This nanostructure can be assigned to type IV with hysteresis loop [48]. The isotherm with hysteresis loop establishes meso porous in all the synthesized nanostructures. Thus, the composite mixture which contains C, H, O and Na actually modifies and advances the material, hence the massive increase in the surface area and pore volume. This observation can also be supported by Figure 8(a), (b), (c) which shows a large spike in volume and area in the range pore diameters <40 nm when compared with undoped material. However, these results do not explain the total increase in BET surface area (as shown in Figure 8(d)) that appears to be also a result of a large increase in "external" surface area. It could very well be a result of the hierarchical structure observed on the SEM which created additional surface area on the outside surface and in the established pores. The increased pore volume before and after doping Gd is likely a result of "leaching" of the material. Surface area and porosity properties of pure α-Sb_2O_4 and Gd: α-Sb_2O_4 (10 wt.%) nanostructures are summarized in Table 6.

3.6. Scanning electron microscopy (SEM) studies

The SEM (scanning electron microscopy) images are very helpful to examine surface morphology and inner structure of the synthesized

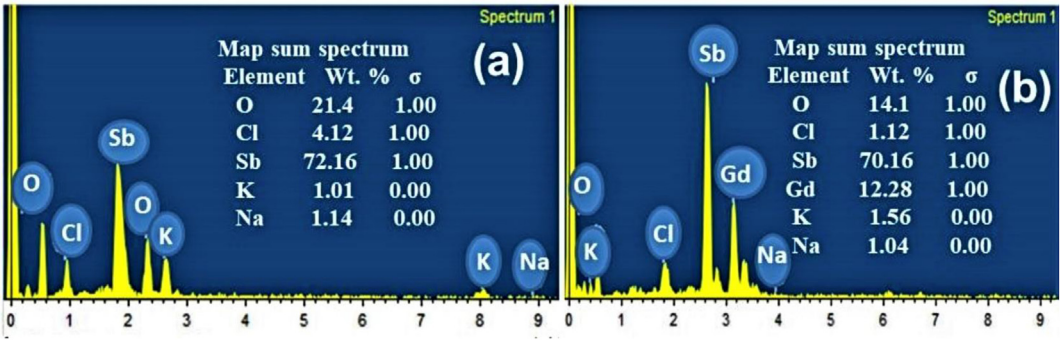

Figure 7. EDS elemental analysis of (a) pure α-Sb_2O_4 NS and (b) Gd: α-Sb_2O_4 (10 wt.%) NS.

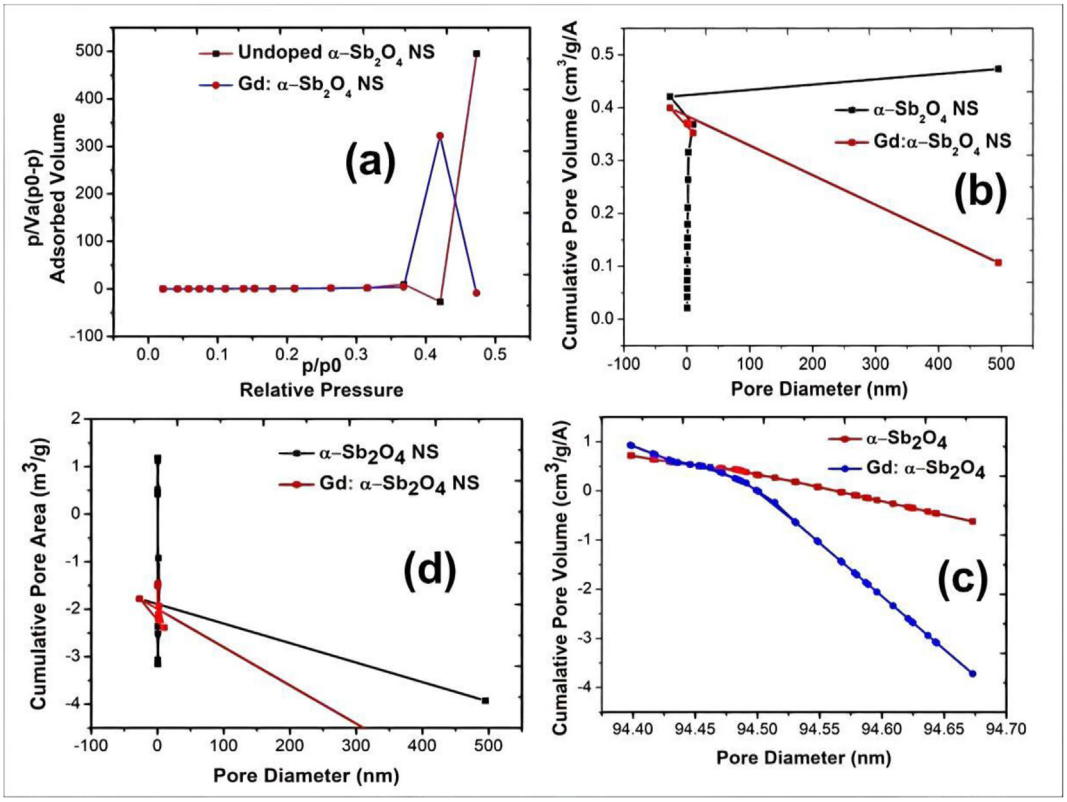

Figure 8. (a) Adsorbed volume Vs relative pressure of pure α-Sb_2O_4 and Gd: α-Sb_2O_4 (10 wt.%) NS (b) and (c) cumulative pore volume Vs pore diameter of pure α-Sb_2O_4 and Gd: α-Sb_2O_4 NS (d) cumulative pore area Vs pore diameter of pure α-Sb_2O_4 and Gd: α-Sb_2O_4 NS.

Table 6. Surface area and porosity properties of Gd: α-Sb_2O_4 (10 wt.%) NS.

Parameters	pure α-Sb_2O_4 NS	Gd: α-Sb_2O_4 (10 wt.%) NS
BET Surface area (m^2/g)	50.5841 ± 0.3692	151.4634 ± 2.0611
Micro pore area (from t-Plot) (m^2/g)	14.6686	62.8486
Pore volume (<179 nm) (cm^3/g)	0.07412	0.12542
Micro pore volume (cm^3/g)	0.003064	0.01674
average pore diameter (nm)	17.4650	10.5797

materials. SEM images of the as synthesized Gd: α-Sb_2O_4 NS with different magnifications as shown in Figure 9. As a result of well dispersion of the Gd NPs sandwiched between pure Sb_2O_4 NS (Figure 9(a)) resulted into agglomerated crystal morphology with proper orientation and distribution. Apparent morphology of the as synthesized Gd: α-Sb_2O_4 NS as can be seen in Figure 9 with average grain size estimated to be ~75 nm, grain diameter ~85 nm, grain boundary distance ~110 nm, width ~34 μm respectively. Morphology and distribution of the Gd: α-Sb_2O_4 (5 wt.%) (Figure 9(b) NS has grain size of ~69 nm and NPs distribution largely dependent on the different synthetic approaches such as co-precipitation, hydrothermal, microwave irradiation etc. In most of the cases NS does not form recognizable structure. Crystal morphology of the Gd: α-Sb_2O_4 NS (5 wt.%) showed flower/flake-like and hierarchical shape having NPs appeared with less agglomeration (Figure 9). However, Gd: α-Sb_2O_4 NS (8 wt.% and 10 wt.%) exhibit (Figure 9 (c) and (d)) complete agglomeration having particle size estimated to be ~ 7–80 nm which is in good covenant with the present investigation results. Surface morphology of the Sb_2O_3 NS becomes concave or convex shaped rather than being in the planar which was theoretically discussed in the literature [49]. Pure α-Sb_2O_4 consisting of oxygen vacancies in the crystal surface which plays vital role during electrochemical reactions [50, 51]. Such sites can trap the other gaseous elements and react with O^{2-} which intern causes increased oxidation during electrochemical reaction. In summary, the layered form of the surface nanostructured morphology, oxygen deficiencies in α-Sb_2O_4 effectively explain electrochemical nature of the NS. Gd: α-Sb_2O_4 NS oriented completely in different form as compared with morphology of pure α-Sb_2O_4 NS which was reported in literature [52]. Overall from the top view of the SEM images it can be concluded that orthorhombic Gd: α-Sb_2O_4 NS formed with more agglomeration of the NPs in the nano-matrix. EDX composition (atomic weight ratio and net ratio) of different metal/metal oxides i.e. Sb, O, K, Fe etc. and the atomic % of Sb and O are 68.09% and 20.15% as presented in Table 7.

3.7. Sample preparation of Gd: α-Sb_2O_4 NS (x = 5, 8 and 10 wt.%)

Principle of cyclic voltammetry involves application of potentials across the electrodes in both directions and finding the total current gain. Redox processes involve the liberation of cations and anions into the solvent and their quantitative determination can be done using three electrode systems. Samples or NS needs to be tested for their solubility in organic solvents like ethanol, methanol, acetonitrile etc. Ammonium salts in aqueous solution increases homogeneity, high solubility, and conductivity. KOH/NaOH aqueous solution of different molarity can also be used as electrolytes. The electrolytes must have greater stability towards redox reactions taking place in the system and can be used as common solvent to obtain homogeneous solution with the solute. Some of the commonly used solvents like tetra butyl ammonium (0.1–0.3 M) dissolved in N–N-dimethyl formamide (DMF), dichloromethane (DCM), acetonitrile, lithium salts like lithium perchlorate ($LiClO_4$), tetra butyl ammonium bromide (TBAB) in DMF are widely used. In the present study, 6 M KOH aqueous solution used as electrolyte. Ag/AgCl electrode as reference, Pt (2 mm thickness) and 2 mm glassy carbon electrode act as working electrodes. Experiments were performed under inert atmosphere (Ar) and electron migration happens from the electrode surface to the solvent to compensate the charge-discharge processes. Different solvents were used and CV results are compared and best suited solvent used for the analysis of the experiments are employed. In the present investigation 6 M KOH finds better solvent as compared with other solvent systems.

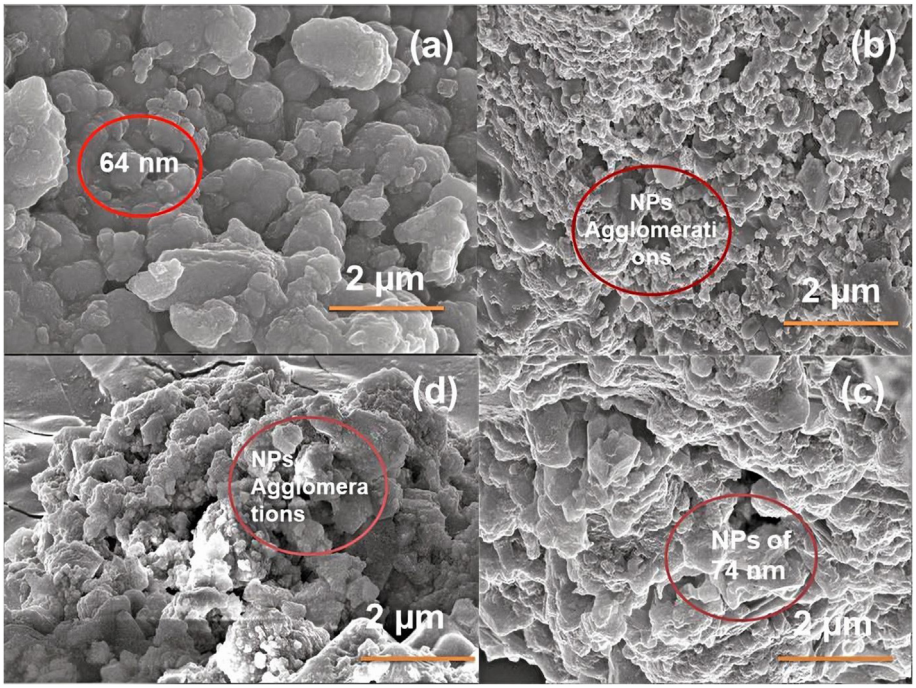

Figure 9. SEM morphology of (a) pure α-Sb_2O_4 NS (b) Gd: α-Sb_2O_4 (5 wt.%) NS (c) Gd: α-Sb_2O_4 (8 wt.%) NS and (d) Gd: α-Sb_2O_4 NS (10 wt.%) NS.

Table 7. EDX compositions of Gd: α-Sb_2O_4 (10 wt.%) NS with their Z, A and F values.

Element	Weight %	Atomic %	Net. Intl	Error %	K Ratio	Z	A	F
Mg	0.34	0.40	0.35	14.08	0.0028	0.7653	0.6654	1.001
Gd	10.85	10.85	10.85	6.16	0.2186	0.5689	1.0428	1.000
K	1.08	1.34	1.28	56.37	0.0144	0.7232	0.9411	1.015
Sb	68.07	68.09	68.07	13.09	0.4143	0.7176	0.9987	1.013
O	20.1120.15	20.28	2.05	0.4258	0.6587	0.8741	1.004	
Fe	0.35	0.38	0.37	9.99	0.0080	0.7502	0.9974	1.015

3.8. Electrochemical (EC) measurements

3.8.1. Galvanostatic charge-discharge (GCD) and cyclic voltammetry (CV) studies

To explore the capacitive performance of the as-synthesized flower/flake like NS, cyclic voltammetry (CV) was examined in three electrode system and distinctive CV profiles of the Gd: α-Sb_2O_4 NS conducted in scan rate of 10 mV/s to 100 mV/s as displayed in Figure 10. CV profiles of Gd: α-Sb_2O_4 electrode signifies Faradaic nature of charge storage mechanism. The ability of a body to store electrical charge termed as capacitance and the energy stored can be calculated from the Eq. (6).

$$\Delta Q = C \times \Delta U \tag{6}$$

Where, Q-charge stored (expressed in coulombs, C, or mAh) and U-width of the voltage window (V). The term "pseudo capacitance" used commonly in the field of electrochemical super capacitor in order to designate the electrode materials that have the signature of capacitive electrode. Such electrodes (RuO_2 and MnO_2) exhibit linear response towards charge stored and width of the potential window. However different mechanism of charge storage originates from the hybrid materials [53, 54, 55]. Conway stated that "electrochemical double layer capacitance" arises as result of charge storage in the material which occurs electrostatically (non-Faradaic) whereas, pseudo capacitance arises at the electrode surface as a result of charge/discharge similarly in case of a battery. It is Faradaic in origin wherein, charge transfer take place across the double layer but capacitance arises from the thermodynamic relation between charge acceptance (Δq) and change in potential (ΔV). The derivative dq/dV is equivalent to capacitance. The prospectus level of hybrid nano scale materials with their energy density or power density of a batteries and cycle life of a super capacitor is an exciting direction yet to be realized. Clear distinction can be made between batteries and super capacitor when nano sized materials are used. When battery is prepared from nano sized materials, their power density increases because of the short transport for the ions and electrons [56]. However, transformation into oxide super capacitor does not occur since, Faradaic redox peak and galvanostatic peaks remain battery type. Pronounced redox peak in voltammetry indicates pseudo capacitance provided, peak voltage differences are small with increase in the sweep rate. In batteries cyclic voltamograms are characterized by large Faradaic redox peaks with large voltage difference (generally 0.1–0.2 V) between oxidation and reduction [57]. As a result of phase transition between oxidation and reduction peaks and the presence of two phases characterized by voltage plateau in galvanostatic experiments. Varakin *et al* [58] reported unexpected improve in the energy storage properties in capacitors when combined with different electrode materials, one with carbonic electrode and other is capacitive nickel oxide electrode. In such cases capacitance of the electrode increases to 8–10 times. Nonetheless the strategies are effective in accommodating volume change and enhancing the electronic and ionic properties of the NS, it becomes challenging to enhance the long cycle life and high rate capabilities. This is due to the largely the fact that nano architecture Sb tend fracture to aggregate dissociate from the Gd network and decreases electronic transportation path during charging and discharging process [59]. However, agglomerations of Sb NPs during charging-discharging process results in kinetic degradation and poor cyclic performance [60]. During Sb alloying process, large volume variation results in loss of electrical contact for active materials and generation of solid-electrolyte interface (SEI) layer. In asymmetric capacitor cycle life is achieved by limiting the Faradaic depth of voltage discharge. Since, the materials are dissimilar in their operating voltage and can be increased significantly. Hybrid electrodes can be used to pair with different materials in different charge storage behaviour (one capacitive and another Faradaic). Thus asymmetric electrodes covers wide range of electrode combinations since, it can be used for super capacitor with different mass loadings. In CV the redox peaks are typical Faradaic battery type electrode which distinctly different from the behaviour of true pseudo capacitive electrodes.

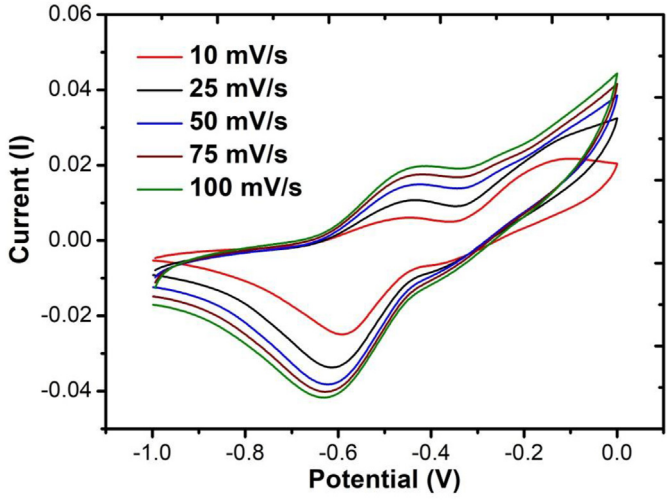

Figure 10. Voltammetric profiles of Gd: α-Sb_2O_4 NS (10 wt.%) with potentials of 10 mV/s to 100 mV/s.

The Faradaic reactions occurring in Gd: α-Sb_2O_4 NS are depicted as below (Eqs. (7), (8), (9), and (10))

$$Sb_2O_4 + 4H^+ + 4e^- \leftrightarrow 2SbOOH + 2OH^- \tag{7}$$

$$Gd_2O_3 + 2H^- + 2e^- \leftrightarrow 2GdOOH + OH^- \tag{8}$$

$$Sb_2O_4 + xH^+ + x e^- \leftrightarrow Sb_2O_{4-x} + (OH)_x \tag{9}$$

$$Gb_2O_3 + xH^+ + + xe^- \leftrightarrow Gd_2O_{3-x}(OH)_x \tag{10}$$

In order to determine energy storage properties of the Gd: α-Sb_2O_4 (10 wt.%) NS, we carried out cyclic voltammetry (CV) (Figure 10) and galvanostatic charge discharge cycles (GDC) using conventional electrode set up. CV exhibited more distinct and sharper peaks due to facile migration of Gd^{+3} ions creating defect in the NS. Sharp peak observed at 10 mV/s due to change in the structural transformation during the electrochemical reaction. The second peak (25 mV/s) is less sharper which is possibly due to greater kinetics of the reaction achieved during CV. This phenomenon is common in structural types of anodes where material undergoes thermodynamic relaxations [61]. Three electrode

systems consist of counter electrode Pt, Ag/AgCl (3M NaCl) as reference electrode and core shell of Gd: α-Sb_2O_4 NS coated on a glass substrate (uniform surface area of 1 cm^2 approximately 1.5 mg of the sample) were used to investigate the electrochemical behaviour of Gd: α-Sb_2O_4 NS. We used 6 M KOH aqueous solution as electrolyte. CV and galvanostatic charge-discharge (GCD) cycles performed with voltage window from 0–2 V vs. Ag/AgCl with a scan rate of 10 mV/s to 100 mV/s of the sample under investigations. GCD cycles performed under voltage window of 0–1 V with current density of 0.1 A/g to 2 A/g. Electrochemical (EC) impedance analysis was carried out using electrochemical impedance analyser (EIS). The investigation carried out with voltage of 2 V filter paper in between containing ~70 wt.% of Gd: α-Sb_2O_4 NS, 10 wt.% of PVDF (poly vinylidine fluoride), 20 wt.% of acetylene black and 6M aqueous KOH solution used as electrolyte. Current densities were calculated using mass of the active materials.

We also carried out GCD cycles in order to understand the charge retention capacity of the electrode and cyclic stability of the Gd: α-Sb_2O_4 NS. Typical GCD profiles of the electrode were conducted at numerous current densities starting from 0.1 A/g to 2 A/g as displayed in Figure 11(a), (b), (c), (d), Figure 12(a) and (b) respectively. Nearly symmetrical GCD curves at all current densities showed good Columbic efficiency and high reversible nature of the electrochemical reactions occurring at Gd: α-Sb_2O_4 electrode. During galvanostatic process, NS rendered specific current of 0.15 A/g, specific capacitance close to 958 mAh/g for 1000 cycles. Cyclic performance of the Gd: α-Sb_2O_4 NS at lower and higher currents presented in the Figures 11 and 12 with the anticipation of understanding mechanism of energy storage we carried out phase transformation to understand morphological evolution of the Gd: α-Sb_2O_4 NS [62]. The planar electrode with aqueous electrolyte in contact with each other and energy is stored in contact with electrode surface by means of physical adsorption. The total capacitance can be given as (Eq. (11))

$$C_T = C_{DL} + C_F \tag{11}$$

Where, Rf –resistance due to Faradaic reaction; C_F-capacitance due to Faradaic reaction and C_{DL}-capacitance in double layer (negligibly small).

In general, redox reaction involving proton and in basic solution can be written as (Eq. (12))

$$X + H^+ + e^- \leftrightarrow P \tag{12}$$

Where, X-reactant, P-product. The equilibrium constant and activities of the proton related to the functional group at the surface as presented in Eq. (13).

$$K = \frac{a_R}{a_A\, a_{H^+}} \tag{13}$$

Where, $a_R = N(\theta)$ and $a_A = (N-1)(\theta)$, N stands for surface density of the O_2 containing hybrid NS, (θ) represents fraction of the reduced state of the chemicals. Faradaic capacitance is enhanced as the number density of oxygen functional group and N value increases. This trend agrees with experimental observation having more oxygen functional groups take part in the Faradaic reaction, encompassing larger electrochemical energy. In contrast, initial charge and discharge capacities of pure α-Sb_2O_4 NS was found to be 624 mAh/g and consistent rapid delay in the specific capacitance was observed during first 100–200 cycles and reversible cycles show decrease of specific capacity of 74.5 mAh/g with capacity loss up to 68.9% after 200 cycles. After doping with Gd, 50th cycle onwards decrease in the capacity of ~10 mAh/g with only 5.8% loss was observed. The outstanding capacities are Gd/α-Sb_2O_4 NS is illustrated by new and unique crystal structure which allows electrolyte inside the surface of the NS facilitating contact area of the electrode to enlarge and store energy [63, 64]. Nanostructure possessing such enlargement between electrolyte and electrode surface area generally composed of rectangular CV curves as observed with Gd/α-Sb_2O_4 NS (Figure 11) which also indicates good electrochemical nature. Strong redox peak attributed to agglomerated flake morphology of Gd/α-Sb_2O_4 NS covered with a layer of α-Sb_2O_4. Gd^{+3} ion insertion or presence of protons increases the current density of the bimetallic oxide NS. The high current density of Gd/α-Sb_2O_4 NS compared with pure Gd_2O_3, pure α-Sb_2O_4 NS. Specific capacitance was calculated using the below formula (Eq. (14)).

$$C = \frac{(I\,\Delta t)}{(\Delta V m)} \tag{14}$$

Where, C-specific capacitance, i-constant current, Δt-discharge time, ΔV-potential range, and m-mass of the sample [65]. Specific Capacitance, Rs, Rp, CPE values of Gd: α-Sb_2O_4NS summarized in Table 8.

Gd NPs anchored non-uniformly in the α-Sb_2O_4 NS providing strong interaction between Gd and Sb NPs. This strong interaction avoids structural collapse during cycling, avoids aggregation during current conduction as can be clearly seen from the Figure 10. Nyquist plots which run parallel as the time elapsed during electrochemical reactions and become ultimately beneficial by undergoing reversible conversion with less capacity loss and alloying reaction between Gd and Sb NPs. The synergistic effect in the morphology of the NS resulted in high energy storage inside the NS and can be used in super capacitor applications. Specific capacitance of 958 mAh/g at current density of 0.15 A/g observed for Gd: α-Sb_2O_4 NS which are compared with previous reported literature of different nanocomposites and summarized in Table 9. The ohmic voltage drops in the discharge curves for pure Sb_2O_4 NS were stabilized due to the migration of Gd^{+3} ions into Sb_2O_4 NS. Cycle performance, stability, retention of Gd: α-Sb_2O_4 NS (10 wt.%) evaluated based on observed capacitance over charge-discharge cycles up to 1000 cycles, capacitive retention Vs charge-discharge cycles, Initial charge-discharge cycles and final charge-discharge cycles as displayed in Figure 13(a), (b), (c) and (d) respectively. In the present investigation CV was performed with scan rate of 10, 25, 50, 75 and 100 mV/s and CV curve maintains rectangular shape even at scan rate of 100 mV/s exhibiting good charge-discharge properties and rate capability, CV curves possessing enlarged voltage window generally improves energy storage and power density of the Gd: α-Sb_2O_4 NS. Energy density (E) and power density (P) can be calculated using the following Eqs. (15) and (16).

$$E = \frac{1}{2}(CV)^2 \tag{15}$$

$$P = \frac{E}{t} \tag{16}$$

Where, C-specific capacitance, V- working voltage of the super capacitor, and t-elapsed times to discharge [66]. Mass ratio of the electrodes can be calculated from the below Eq. (17).

$$\frac{m^+}{m^-} = \frac{C^-\Delta V^-}{C^+\Delta V^+} \tag{17}$$

Where, C^+ and C^- represents specific capacitance of the +ve and – ve electrodes and ΔV^+ and ΔV^- are the potential windows for + ve and – ve electrodes respectively.

In CV curves the amount of charge stored depends on the current response (i) and sweep rate (υ) which is given by the Eq. (18).

$$i = C\upsilon^{\frac{1}{2}} \tag{18}$$

The total charge stored may be the combination of three parts, Faradaic contribution as a result of interaction of charges, Faradaic reactions involving surface atoms and charges stored and non-Faradaic by the double layer effect. Consequently NS with large porosity and higher surface area needs to be chosen for obtaining higher capacitance and operating potential depends on the electrolyte and nature of the electrode materials.

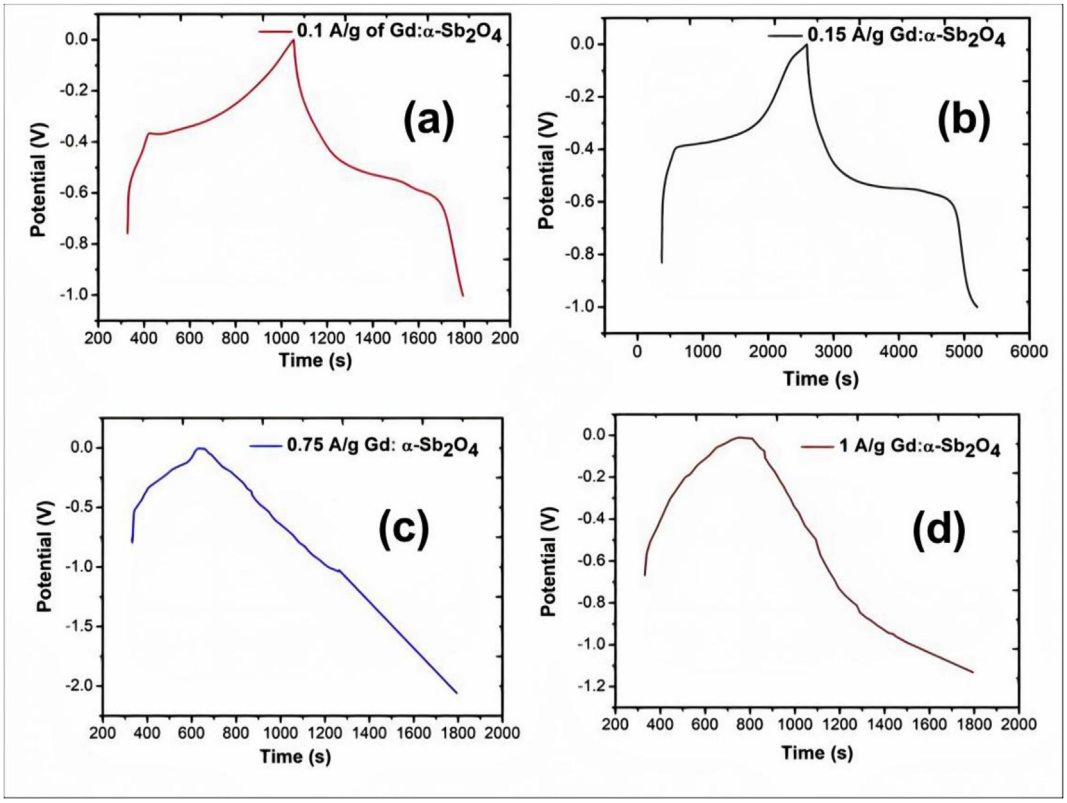

Figure 11. Galvanostatic charge discharge cycles of Gd: α-Sb_2O_4 NS (10 wt.%) at current densities of (a) 0.1 A/g (b) 0.15 A/g (c) 0.75 A/g and (d) 1 A/g respectively.

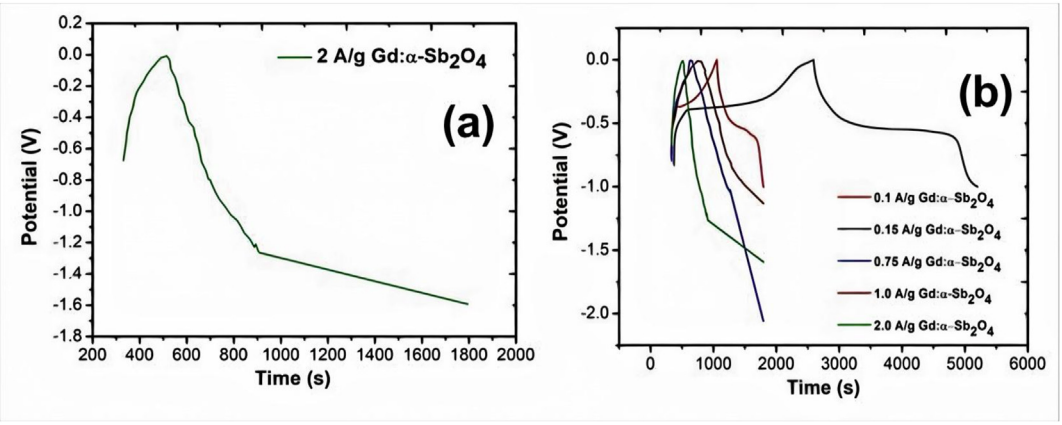

Figure 12. Galvanostatic charge discharge (GCD) cycles of Gd: α-Sb_2O_4NS (10 wt.%) at current densities of (a) 2 A/g (b) Overlay of GCD cycles sweep from 0.1 A/g to 2 A/g.

Table 8. Specific Capacitance, Rs, Rp, CPE values of Gd: α-Sb_2O_4 NS.

Nano structures	Specific Capacitance (mAh/g) at 0.15 A/g	R_s (Ω)	R_p (Ω)	CPE (mF)	C (mF)	W (m Ω)
Gd: α-Sb_2O_4 (10 wt.%)	958	0.978	1.67	9.34	38.4	0.678

3.8.2. Nyquist and electrochemical impedance spectroscopy (EIS) studies

The galvanostatic charge/discharge profiles of as-synthesized Gd: α-Sb_2O_4 NS in cycles 100, 200, 500, and 1000 at current density of 0.1, 0.15, 0.75, 1, 2 A/g in the voltage window of 0–2 V. Gd: α-Sb_2O_4 (10 wt.%) NS exhibited two reaction plateaus located at 1.10 V and 0.6 V and slope of the region below 0.4 V during the discharge process. During the first 100 cycles declined region in between 0.9 V to 0.4 V in the discharge curve appears to replace the plateaus located at 1.40 V.

The variation of real part of the impedance is plotted with respect to frequency and variation of imaginary part of the impedance is plotted with respect to frequency as displayed in Figure 14(a) and (b). The impedance response shows a strong relaxation at low frequencies. The data was fit to Cole –Cole response function and calculated using Eq. (19).

$$z' = R_e + \frac{R_b}{1 + (\varpi\tau)^2} \tag{19}$$

Where R_b-bulk resistance and τ-relaxation time. The bulk resistance or the internal resistance of the cell obtained from this analysis were 6.4 Ω, 172 Ω, 90 k Ohm and relaxation time were 7 s, 172 s and 481 s

Table 9. Literature reports of various nanostructures, their preparation method, cyclic stability, capacitance with present study of Gd: α-Sb_2O_4 NS (10 wt.%).

Electrode Material	Preparation method	Cyclic Stability	Capacitance (F/g)	References
$NiCo_2O_4$–NiO	Galvanostatic	–	82.1	[71]
Na-doped SCO	CV/Galvanostatic	–	519.80/319	[72]
Co_3O_4 nanotubes	Chemical deposition	500 cycles	273	[73]
MnO_2/RGO composite	Electrochemical deposition	5000 cycles	125.93	[74]
K–SCO/ K–$SrCu_2O_2$	CV/Galvanostatic	–	735.73/438	[75]
Gd: α-Sb_2O_4 NS	Co precipitation	1000 cycles	958 mAh/g	Present Study

respectively for 5 wt.%, 8 wt.% and 10 wt.% Gd doped samples. The slow transport is the characteristic of the diffusion dominant activation of ions or porous media [67]. To understand the dominance of the dissipative processes the imaginary part of the impedance was plotted and fit the imaginary part of the Cole-Cole response function. As depicted in the real part of the data the relaxation frequencies were shorter indicating diffusion dominant transport.

The Nyquist plot displayed in Figure 15(a) and (b) exhibited dominant diffusive process as modeled through a Warburg component. As observed in the Cole –Cole relaxation analysis the internal resistance of the system was observed to be less. The values obtained from pure Nyquist analysis are 0.2 Ohm, 0.4 Ω 0.5 Ω respectively for 5%, 8% and 10% Gd doped samples which are less than the values obtained through Cole- Cole relaxation analysis. This is typically observed in low resistance electrodes [68, 69]. Typical simulated equivalent circuit model (ECM) as displayed in Figure 15(c). Electron delocalization could be one of the significant resistance for the lower value of IR [70]. Furthermore, with increase in Gd concentration total bulk seemed to increase hindering the electron flow across the framework. It is important to note that the equivalent circuit fits for the partial data set (Warburg short kind, not the infinite R–C pure diffusive kind) as shown in Figure 15(c) but in the extended low frequency range the diffusion dominates the bulk transport.

3.8.3. Relation between phase angle and time of Gd: α-Sb_2O_4 NS

Electrochemical impedance spectroscopy (EIS) was performed to understand electrochemical characteristics of Gd: α-Sb_2O_4 NS (10 wt.%). Gd: α-Sb_2O_4 NS presents Nyquist plots (Figure 15) with smaller semi-circle, all the plots run in parallel with ohmic resistance which varies uniformly without the loss of capacity which is correlated to the charge transfer from Gd^{+3} ions and O^{2-} ions on to the surface of α-Sb_2O_4 NS which intern confirms the dominant electrochemical reactions. The phase angle increases and after the elapse of 250 s it decreases considerably indicating Gd^{+3} ions from the surface of α-Sb_2O_4 NS transferred

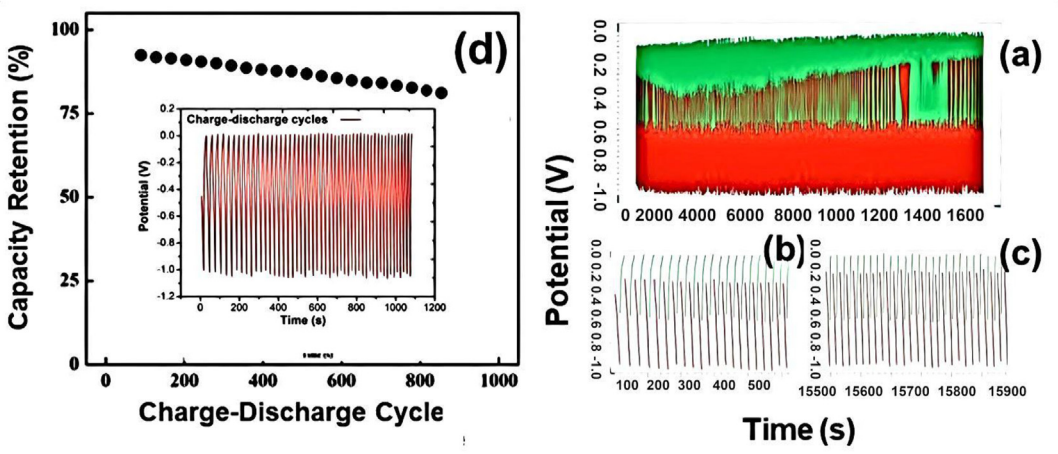

Figure 13. (a) 1000 GCD cycles for Gd: α-Sb_2O_4 (10 wt.%) NS in 6 M KOH (b) Initial charge-discharge cycles (c) final charge-discharge cycles (d) capacitive retention Vs charge-discharge cycles.

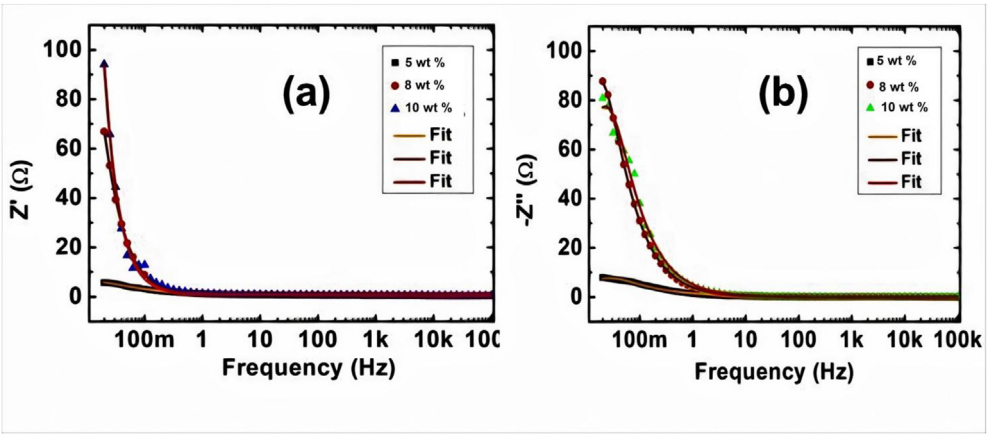

Figure 14. (a) Variation of real part of the impedance with frequency, the data was fit to Cole –Cole response function (b) Variation of imaginary part of the impedance with frequency, the data was fit to Cole –Cole response function.

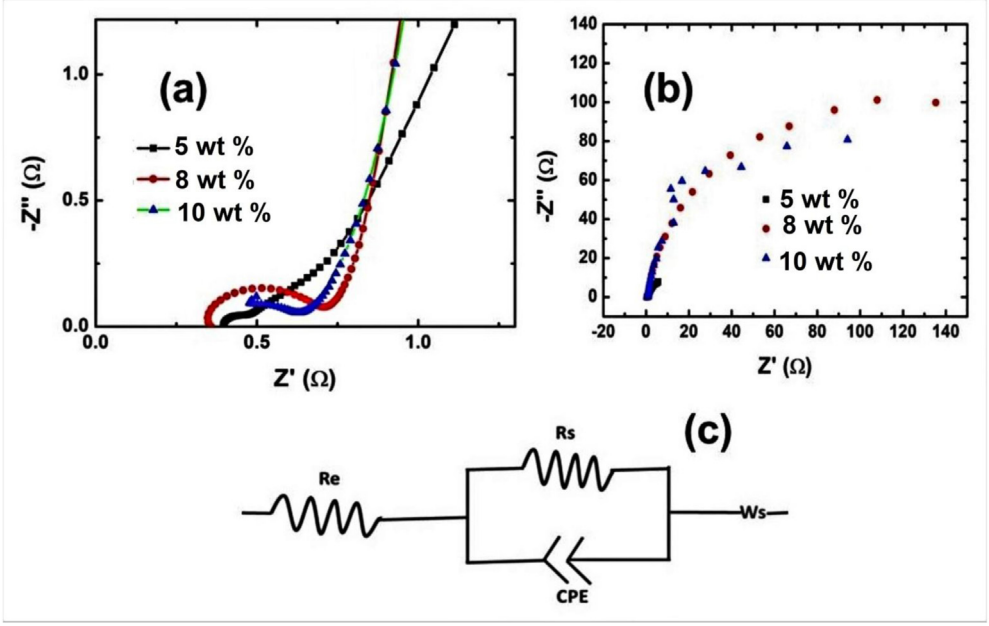

Figure 15. (a) and (b) Nyquist plots of Gd: α-Sb_2O_4 NS with increased concentration of Gd (c) Equivalent circuit model (ECM) of Gd: α-Sb_2O_4 NS.

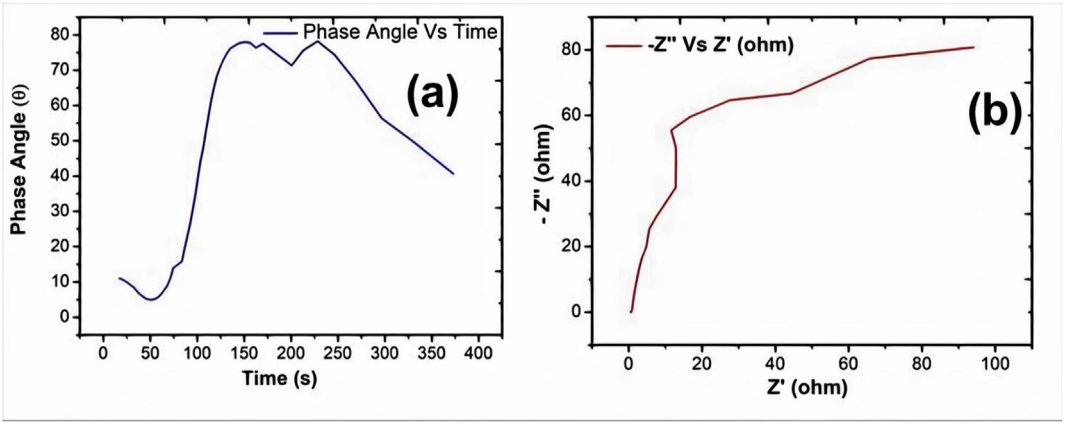

Figure 16. (a) Plot of phase angle Vs time for Gd: α-Sb_2O_4 (10 wt.%) NS (b) Z ″ Vs Z′ curve of Gd: α-Sb_2O_4 NS (10 wt.%).

effectively [71, 72]. Plot of phase angle versus time elapsed as shown in Figure 16(a) and Z″ (imaginary) Vs Z′ (real) resistivity curve of Gd: α-Sb_2O_4 NS (10 wt.%) as depicted in Figure 16(b). Initially the phase angle varies slowly and as the electrochemical reaction time increases phase angle also increases indicating reaction of O^{2-} ions from the surface of the α-Sb_2O_4 NS and transfer of electrons into the α-Sb_2O_4 NS [73]. Magnitude of Z′-intercept correlates to the equivalent series resistance Rs, which includes the electrical resistance of electrodes. Resistance values obtained are 1.678 Ω for Gd_2O_3 NPs, 1.032 Ω for α-Sb_2O_4 NPs and of Gd: α-Sb_2O_4 (10 wt.%) NPs has 0.748 Ω respectively. Low charge transfer and electrical resistance of the NS enable the formation of large capacitance and good rate of discharge and recharge cycles [74, 75].

4. Conclusion

In this work, electrode was constructed from flower/flake like Gd_x: α-Sb_2O_4 (x = 5, 8, and 10 wt.%) NS using cost effective co precipitation method. The as-prepared electrode was systematically investigated by XRD, SEM, SEM EDX, BET, EDS, UV-Visible, and XPS spectroscopic techniques. X-ray diffraction pattern revealed orthorhombic crystal structure of Gd_x: α-Sb_2O_4 electrode, crystallinity varies in between 38.31 nm to 49.47 nm. Flake/flower like morphology, abundant active sites, high electrical conductivity and energy storage significantly enhance electron/charge transfer and energy storage capacity of the nanostructure. Optical absorptivity measurement confirmed blue shift in the spectrum due to overloading of Gd^{+3} ions inside α-Sb_2O_4 NS intern formation of defect in the lattice and facilitates easy transfer of oxygen ions and electrons to the surface of the NS. Direct optical band gap (E_g) was found to be 3.16 eV. Electro chemical performances of Gd_x: α-Sb_2O_4 NS investigated in three electrode system in basic 6M KOH as electrolyte. The Gd_x: α-Sb_2O_4 (10 wt.%) electrode displays excellent electrochemical capacitance of 958 mAh/g at 0.15 A/g. Notably, Gd_x: α-Sb_2O_4 NS owns outstanding cyclic

stability of 86.5% after 1000 cycles. These good electrode potentials pave new method for practical applications of Gd_x: α-Sb_2O_4 electrode.

Declarations

Author contribution statement

Vinayak Adimule: Conceived and designed the experiments; Analyzed and interpreted the data; Contributed reagents, materials, analysis tools or data; Wrote the paper.

Basappa C. Yallur: Conceived and designed the experiments; Performed the experiments; Analyzed and interpreted the data.

Malathi Challa: Analyzed and interpreted the data; Wrote the paper.

Rajeev S. Joshi: Performed the experiments; Wrote the paper.

Funding statement

This research did not receive any specific grant from funding agencies in the public, commercial, or not-for-profit sectors.

Data availability statement

Data will be made available on request.

Declaration of interests statement

The authors declare no conflict of interest.

Additional information

No additional information is available for this paper.

Acknowledgements

Authors are thankful to IIT Kanpur for SEM, SEM EDX, BET, EDS and XPS analysis, Centre for Advanced Material Research, MSRIT, Bangalore, Karnataka, India for XRD, UV-visible and elemental compositional analysis. Centre for Nano and Material Sciences (CNMS) Bangalore, Karnataka, India for electrochemical studies.

References

[1] B.E. Conway, Electrochemical Super Capacitors Scientific Fundamentals and Technological Applications Chapter 1, Kluwer Academic, Dordrecht/Plenum, New York, 1999.

[2] A. F Burke, T. C Murphy, D. H Goughtly, B. Vyas, T. Takamura, J.R. Huff, Materials for Energy Storage and Conversion: Batteries, Capacitors and Fuel Cells, Materials Research Society, Pittsburgh, USA, 1995, p. 375.

[3] J. H Lee, S. H Lee, Applications of novel carbon/$AlPO_4$ hybrid-coated $H_2Ti_{12}O_{25}$ as a high performance anode for cylindrical hybrid super capacitors, ACS Appl. Mater. Interfaces 8 (42) (2016) 28974–28981.

[4] J. H Lee, H. K Kim, E. Baek, M. Pecht, S.H. Lee, Y. H Lee, Improved performance of cylindrical hybrid super capacitor using activated carbon/niobium doped hydrogen titanate, J. Power Sources 301 (2016) 348–354.

[5] B. E Conway, W.G. Pell, Double-layer and pseudo capacitance types of electrochemical capacitors and their applications to the development of hybrid devices, J. Solid State Electrochem. 7 (2003) 637–644.

[6] W.G. Pell, B.E. Conway, Peculiarities and requirements of asymmetric capacitor devices based on combination of capacitor and battery-type electrodes, J. Power Sources 136 (334) (2004) 334–345.

[7] J.P. Zheng, The limitations of energy density of battery/double-layer capacitor asymmetric cells, J. Electrochem. Soc. 150 (A484) (2003).

[8] Y. Yi, H.W. Shim, S.D. Seo, M.A. Dar, D.W. Kim, Enhanced Li- and Na-storage in Sb-graphene nanocomposite anodes, Mater. Res. Bull. 76 (2016) 338–343.

[9] H.Y. Lu, F. Wan, L.H. Jiang, G. Wang, X.L. Wu, Graphene nano sheets suppress the growth of Sb nanoparticles in an Sb/C nanocomposite to achieve fast Na storage, Part. Syst. Char. 33 (4) (2016) 204–211.

[10] X. Zhou, Z. Zhang, X. Lu, X. Lv, G. Ma, Q. Wang, Z. Lei, Sb_2O_3 Nanoparticles anchored on graphene sheets via alcohol dissolution-re precipitation method for excellent lithium-storage properties, ACS Appl. Mater. Interfaces 9 (40) (2017) 34927–34936.

[11] Y. Tan, L. Chen, H. Chen, Q. Hou, X. Chen, Synthesis of a symmetric bundle-shaped Sb_2O_3 and its application for anode materials in lithium-ion batteries, Mater. Lett. 212 (2018) 103–106.

[12] X.Z. Zhou, Z.F. Zhang, J.W. Wang, Q.T. Wang, G. F Ma, Z.Q. Lei, Sb_2O_4/reduced graphene oxide composite as high-performance anode material for lithium-ion batteries, J. Alloys Compd. 699 (2017) 611–618.

[13] X. Z Zhou, Z. F Zhang, X. H Xu, J. Yan, G.F. Ma, Z.Q. Lei, Anchoring Sb_6O_{13} nano crystals on graphene sheets for enhanced lithium storage, ACS Appl. Mater. Interfaces 8 (51) (2016) 35398–35406.

[14] H. Hou, M. Jing, Z. Huang, Y. Yang, Y. Zhang, J. Chen, Z. Wu, X. Ji, One-dimensional rod-like Sb_2S_3-based anode for high-performance sodium-ion batteries, ACS Appl. Mater. Interfaces 7 (34) (2015) 19362–19369.

[15] Q. Sun, Q.Q. Ren, H. Li, Z.W. Fu, High capacity Sb_2O_4 thin film electrodes for rechargeable sodium battery, Electrochem. Commun. 13 (12) (2011) 1462–1464.

[16] F. Klein, B. Jache, A. Bhide, P. Adelhelm, Conversion reactions for sodium-ion batteries, Phys. Chem. Chem. Phys. 15 (2013) 15876–15887.

[17] D. Orosel, P. Balog, H. Liu, J. Qian, M. Jansen, Sb_2O_4 at high pressures and high temperatures, J. Solid State Chem. 178 (9) (2005) 2602–2607.

[18] S. Liu, B. Wen, W. Jiang, C. Liu, W. Ding, N. Wang, W. Chai, Influence of calcination temperature on the structure, morphology and composition of micro α-Sb_2O_4 crystals, Ceram. Int. 40 (10) (2014) 15991–15995.

[19] N. Yadav, M. Nagar, R. Bohra, New sol-gel precursors for binary oxides of antimony, Sb_2O_3 (senarmonite) and α-Sb_2O_4: synthesis and characterization of some ketoximate modified antimony (III) alkoxides, J. Sol. Gel Sci. Technol. 54 (1) (2010) 119–128.

[20] Q. Sun, Q.Q. Ren, H. Li, Z.W. Fu, High capacity Sb_2O_4 thin film electrodes for rechargeable sodium battery, Electrochem. Commun. 13 (12) (2011) 1462–1464.

[21] A. Jamal, M. M Rahman, S. B Khan, M. M Abdullah, M. Faisaal, A. M Asiri, A. Aslam, P. Khan, K. Akhtar, Simple growth and characterization of α-Sb_2O_4: evaluation of their photo-catalytic and chemical sensing applications, J. Chem. Soc. Pakistan 35 (3) (2013) 570–577.

[22] Z. Yi, Q. Han, X. Li, Y. Wu, Y. Cheng, L. Wang, Two-step oxidation of bulk Sb to one dimensional Sb_2O_4 submicron-tubes as advanced anode materials for lithium-ion and sodium-ion batteries, Chem. Eng. J. 315 (2017) 101–107.

[23] Q. Sun, Q.Q. Ren, H. Li, Z.W. Fu, High capacity Sb_2O_4 thin film electrodes for rechargeable sodium battery, Electrochem. Commun. 13 (12) (2011) 1462–1464.

[24] X.Z. Zhou, Z.F. Zhang, J.W. Wang, Q.T. Wang, G. F Ma, Z.Q. Lei, Sb_2O_4/reduced graphene oxide composite as high-performance anode material for lithium-ion batteries, J. Alloys Compd. 699 (2017) 611–618.

[25] M. M Rahman, J. Ahmed, Cd-doped Sb_2O_4 nanostructures modified glassy carbon electrode for efficient detection of melamine by electrochemical approach, Biosens. Bioelectron. 102 (2018) 631–636.

[26] H. Xiao, P. Li, F. Jia, L. Zhang, General non-aqueous sol-gel synthesis of nanostructured Sm_2O_3, Gd_2O_3, Dy_2O_3, and Gd_2O_3:Eu^{3+} phosphor, J. Phys. Chem. C 113 (50) (2009) 21034–21041.

[27] M. M Abdullah, Fabrication of ethanol chemical sensors based on as-prepared Gd_2O_3 nanorods by facile hydrothermal routes, J. Colloid. Sci. Biotechnol. 2 (4) (2013) 322–327.

[28] S. Hussain, A.J. Khan, M. Arshad, M.S. Javed, A. Ahmad, S.S. Ahmad Shah, M.R. Khan, S. Akram, Zulfiqar, S. Ali, Z.A. Alothman, G. Liu, Charge storage in binder-free 2D-hexagonal $CoMoO_4$ nano sheets as a redox active material for pseudo capacitors, Ceram. Int. 47 (6) (2020) 8659–8667.

[29] S. Hussain, M. Hassan, M.S. Javed, A. Shaheen, S.S. Ali Shah, M.T. Nazir, T. Najam, A.J. Khan, X. Zhang, G. Liu, Distinctive flower-like $CoNi_2S_4$ nano needle arrays (CNS–NAs) for superior super capacitor electrode performances, Ceram. Int. 46 (16) (2020) 25942–25948. Part A.

[30] S. Hussain, M.S. Javed, S. Asim, A. Shaheen, A.J. Khan, Y. Abbas, N. Ullah, A. Iqbal, M. Wang, G. Qiao, S. Yun, Novel gravel-like $NiMoO_4$ nanoparticles on carbon cloth for outstanding super capacitor applications, Ceram. Int. 46 (5) (2019) 6406–6412.

[31] A. Jamal, M. M Rahman, S. B Khan, M. M Abdullah, M. Faisaal, A. M Asiri, A. Aslam, P. Khan, K. Akhtar, Simple growth and characterization of α-Sb_2O_4: evaluation of their photo-catalytic and chemical sensing applications, J. Chem. Soc. Pakistan 35 (3) (2013) 570–577.

[32] Z.J. Zhang, X.Y. Chen, Biomolecule-assisted hydrothermal synthesis of Sb_2S_3 and Bi_2S_3 nano crystals and their elevated-temperature oxidation behaviour for conversion into α-Sb_2O_4 and Bi_2O_3, J. Phys. Chem. Solid. 70 (7) (2009) 1121–1131.

[33] M. Faisal, S.B. Khan, M.M. Rahman, A. Jamal, Role of ZnO-CeO_2 nanostructures as a photo-catalyst and chemi-sensor, J. Mater. Sci. Technol. 27 (7) (2011) 594–600.

[34] K.A. Aly, N.M. Khalil, Y. Algamal, Q.M.A. Saleem, Estimation of lattice strain for zirconia nano-particles based on Williamson- Hall analysis, Mater. Chem. Phys. 193 (2017) 182–188.

[35] M.S. Pudovkin, P.V. Zelenikhin, V. Shtyreva, Co precipitation method of synthesis, characterization, and cytotoxicity of Pr^{3+}:LaF_3 (CPr = 3, 7, 12, 20, 30%) nanoparticles, J. Nanotechnol. 2018 (8516498) (2018).

[36] G. Vijayaprasath, R. Murugan, Y. Hayakawa, G. Ravi, Optical and magnetic studies on Gd doped ZnO nanoparticles synthesized by co-precipitation method, J. Lumin. 178 (2016).

[37] S. Laurent, D. Forge, M. Port, A. Roch, C. Robic, L. Vander Elst, R.N. Muller, Magnetic Iron oxide nanoparticles: synthesis, stabilization, vectorization, physicochemical characterizations, and biological applications, Chem. Rev. 108 (2008) 2064–2110.

[38] B. Cojocaru, D. Avram, V. Kessler, V. Parvulescu, G. Seisenbaeva, C. Tiseanu, Nanoscale insights into doping behaviour, particle size and surface effects in trivalent metal doped SnO_2, Sci. Rep. 7 (2017) 9598.

[39] S. Roy, S. Bardhan, D. Chanda, A. Maity, S. Ghosh, D. Mondal, S. Singh, S. Das, Cu (II) and Gd (III) doped boehmite nanostructures: a comparative study of electrical property and thermal stability, Mater. Res. Express 7 (2) (2020) 25020–25032.

[40] A. Serafini, L. Lutterotti, S. Gross, S. Gialanella, Characterization of nano grained powder samples using the rietveld method applied to electron diffraction ring patterns, Powder Diffr. 32 (2017) 63–68. http://hdl.handle.net/11311/1045676.

[41] J.P. Allen, J. J Carey, A. Walsh, D. O Scanlon, G. W Watson, Electronic structures of antimony oxides, J. Phys. Chem. C 117 (28) (2013) 14759–14769.

[42] X.R. Li, X.T. Wang, X.B. Ning, J. Lei, J. Shao, W.C. Wang, Y.L. Huang, B.R. Hou, Sb_2S_3/Sb_2O_3 modified TiO_2 photoanode for photocathodic protection of 304 stainless steel under visible light, Appl. Surf. Sci. 462 (31) (2018) 155–163.

[43] S. Das, S. Das, A. Roychowdhury, D. Das, S. Sutradhara, Effect of Gd doping concentration and sintering temperature on structural, optical, dielectric and magnetic properties of hydrothermally synthesized ZnO nanostructure, J. Alloys Compd. 708 (2017) 231–246.

[44] M. Huang, Merging of Kirkendall Growth and Ostwald Ripening: $CuO@MnO_2$ core–shell architectures for asymmetric super capacitors, Sci. Rep. 4 (4518) (2014).

[45] L.,P. Li, P. Zhu, S. Peng, M. Srinivasan, Q. Yan, A.S. Nair, B. Liu, S. Samakrishna, Controlled growth of CuS on electrospun carbon nano fibers as an efficient counter electrode for quantum dot-sensitized solar cells, J. Phys. Chem. C 118 (30) (2014) 16526–16535.

[46] A. Devi, S. Cwik, K. Xu, A.P. Milanov, H. Noei, Y. Wang, D. Barreca, J. Meijer, D. Rogalla, D. Kahn, R. Cross, H. Parala, S. Paul, Rare-earth substituted HfO_2 thin films grown by metal organic chemical vapour deposition, Thin Solid Films 520 (14) (2012) 45124517.

[47] S. Yousefi, B. Ghasemi, M. Tajally, A. Asghari, Optical properties of MgO and $Mg(OH)_2$ nanostructures synthesized by a chemical precipitation method using impure brine, J. Alloys Compd. 711 (2017) 521–529.

[48] S. Iqbal, I. Bibi, S. Ata, S. Kamal, S.M. Ibrahim, M. Iqbal, Gd and Co-substituted $LaNiO_3$ and their nanocomposites with r-GO for photo catalytic applications, Diam. Relat. Mater. 110 (2020) 108119.

[49] P. Gopalakrishnan, H. Manohar, Topotaxy in the oxidation of valentinite, Sb_2O_3, to cervantite, Sb_2O_4, . Pramana 3 (5) (1974) 277–285.

[50] K.A. Abdelouahad, M. Roullet, M. Brun, A. Burrows, C.J. Kiely, J. C Volta, M. Abona, Surface alteration of $(VO)_2$ P_2O_7 by α-Sb_2O_4 as a route to control then-butane selective oxidation, Appl. Catal. Gen. 210 (1) (2001) 121–136.

[51] S. Liu, B. Wen, W. Jiang, C. Liu, W. Ding, N. Wang, W. Chai, Influence of calcination temperature on the structure, morphology and composition of micro α-Sb_2O_4 crystals, Ceram. Int. 40 (10) (2014) 15991–15995.

[52] Z.J. Zhang, X.Y. Chen, Biomolecule-assisted hydrothermal synthesis of Sb_2S_3 and Bi_2S_3 nano crystals and their elevated-temperature oxidation behaviour for conversion into α-Sb_2O_4 and Bi_2O_3, J. Phys. Chem. Solid. 270 (7) (2009) 1121–1131.

[53] S. Ardizzone, G. Fregonara, S. Trasatti, "Inner" and "outer" active surface of RuO_2 electrodes Electrochim, Acta 35 (263) (1990) 263–267.

[54] J.P. Zheng, P.J. Cygan, T.R. Jow, Hydrous ruthenium oxide as an electrode material for electrochemical capacitors, J. Electrochem. Soc. 142 (2699) (1995).

[55] H.Y. Lee, J.B. Goodenough, Super capacitor behaviour with KCl electrolyte, J. Solid State Chem. 144 (220) (1999).

[56] A.S. Arico, P. Bruce, B. Scrosati, J.M. Tarascon, W. van Schalkwijk, Nanostructured materials for advanced energy conversion and storage devices, Nat. Mater. 4 (366) (2005).

[57] B.E. Conway, Transition from "Super capacitor" to "Battery" behaviour in electrochemical energy storage, J. Electrochem. Soc. 138 (1539) (1991).

[58] I. Varakin, A. Stepanov, V. Menukhov, Pat. WO97/07518 and US Patent, Capacitor with a Double Electrical Layer, 1995.

[59] I. Sultana, M.M. Rahman, J. Liu, N. Sharma, A.V. Ellis, Y. Chen, A.M. Glushenkov, J. Antimony-carbon nanocomposites for potassium-ion batteries: insight into the failure mechanism in electrodes and possible avenues to improve cyclic stability, J. Power Sources 413 (2019) 476–484.

[60] Z. Yi, N. Lin, W. Zhang, W. Wang, Y. Zhu, Y. Qian, Preparation of Sb nanoparticles in molten salt and their potassium storage performance and mechanism, Nanoscale 10 (2018) 13236–13241.

[61] T. Yamamoto, T. Nohira, R. Hagiwara, A. Fukunaga, S. Sakai, K. Nitta, Electrochemical behaviour of Sn−Fe alloy film negative electrodes for a sodium secondary battery using inorganic ionic liquid Na [FSA]−K[FSA], Electrochim. Acta 211 (2016) 234–244.

[62] Q. Wang, X. Junqi, W. Yanrui, C. Wang, X. Zhao, G. Shen, Y. Guo, J. Chen, Y. Xia, H. Sun, W. Xie, Electrospun α-Sb_2O_4 nano-flowers for enhanced lithium storage performance,, Sci. Adv. Mater. 11 (3) (2019) 435–442.

[63] X. Z Zhou, Z. F Zhang, X. H Xu, J. Yan, G.F. Ma, Z.Q. Lei, Anchoring Sb_6O_{13} nano crystals on graphene sheets for enhanced lithium storage, ACS Appl. Mater. Interfaces 8 (51) (2016) 35398–35406.

[64] Z. Yi, Q. Han, X. Li, Y. Wu, Y. Cheng, L. Wang, Two-step oxidation of bulk Sb to one dimensional Sb_2O_4 submicron-tubes as advanced anode materials for lithium-ion and sodium-ion batteries, Chem. Eng. J. 315 (2017) 101–107.

[65] M. Sarno, C. Cirillo, E. Ponticorvo, P. Ciambelli, Synthesis and characterization of FLG/Fe_3O_4 nanohybrid super capacitor, Chem. Engg Tran. 32 (43) (2015) 727–732.

[66] M. Sajjad, X. Chen, C. Yu, L. Guan, S. Zhang, D. Zhang, X. Zhou, Z. Liu, High energy density asymmetric super capacitor based on $NiCo_2S_4$/CNTs hybrid and carbon nanotube paper electrodes, J. Mol. Eng. Mater. 7 (1) (2019) 195004–195018.

[67] N. Ogihara, Y. Itou, T. Sasaki, Y. Takeuchi, Impedance spectroscopy characterization of porous electrodes under different electrode thickness using a symmetric cell for high-performance lithium-ion batteries, J. Phys. Chem. C 119 (9) (2015) 4612–4619.

[68] J. Allen. Bard, R. Larry. Faulkner, Electrochemical Methods: Fundamentals and Applications, second ed., 2000, pp. 1–864.

[69] J.R. Macdonald, Impedance spectroscopy, Ann. Biomed. Eng. 20 (1992) 289–305.

[70] R. Parsons, The electrical double layer: recent experimental and theoretical developments, Chem. Rev. 90 (5) (1990) 813–826.

[71] J. Zhang, F. Liu, J.P. Cheng, X.B. Zhang, Binary nickel–cobalt oxides electrode materials for high-performance super capacitors: influence of its composition and porous nature, ACS Appl. Mater. Interfaces 7 (32) (2015) 17630–17640.

[72] H.R. Barai, M. M Rahman, N.S. Lopa, P. Barai, S.W. Joo, Sodium-doped binary strontium-copper oxide as a high-performance electrochemical pseudo capacitive electrode material, J. Electrochem. Soc. 167 (2020) 126516.

[73] G. He, J. Li, H. Chen, J. Shi, X. Sun, S. Chen, X. Wang, Hydrothermal preparation of Co_3O_4 in graphene nanocomposite for super capacitor with enhanced capacitive performance, Mater. Lett. 82 (2012) 61–63.

[74] Z. Li, Y. An, Z. Hu, N. An, Y. Zang, B. Guo, Z. Zhang, Y. Yang, H. Wu, Preparation of a two-dimensional flexible MnO_2/graphene thin film and its application in a super capacitor, J. Mater. Chem. 4 (2016) 10618–10626.

[75] H. R Barai, N. S Lopa, P. Barai, M.M. Rahman, A. K Sarker, S.W. Joo, Binary strontium–copper oxide nanostructures doped with potassium as electrode material for super capacitor application, J. Mater. Sci. Mater. Electron. 30 (2019) 21269–21277.